



Microstructures and Mechanical Properties of Multi-component $\text{Al}_x\text{CrFe}_2\text{Ni}_2\text{Mo}_{0.2}$ High-Entropy Alloys

Qiuxin Nie¹ · Hui Liang¹ · Dongxu Qiao¹ · Zhaoxin Qi¹ · Zhiqiang Cao^{1,2}

Received: 10 February 2020 / Revised: 17 April 2020 / Published online: 17 June 2020
© The Chinese Society for Metals (CSM) and Springer-Verlag GmbH Germany, part of Springer Nature 2020

Abstract

A series of $\text{Al}_x\text{CrFe}_2\text{Ni}_2\text{Mo}_{0.2}$ alloy consisting of FCC + BCC phases have been designed, and their as-cast microstructures and mechanical properties were also investigated with x ranging from 0.6 to 0.9. It was found that with the addition of Al element, the solidified structures changed from dendrite to columnar crystal then back to dendrite again. Moreover, the increased amount of BCC phase resulted in finer and more uniform microstructures of FCC [FeCrNi(Mo)] and BCC (Al–Ni) phases. Tensile yield strength and hardness of alloys showed a similar increasing trend as the volume fraction of BCC phase increased. Both strain hardening rate and strain hardening exponent were calculated to assess the tensile properties of the alloys. It was shown that $\text{Al}_{0.6}\text{CrFe}_2\text{Ni}_2\text{Mo}_{0.2}$ exhibited the most excellent and comprehensive mechanical properties due to its high work hardening ability and stable strain hardening rate. The product of strength and elongation of $\text{Al}_{0.6}\text{CrFe}_2\text{Ni}_2\text{Mo}_{0.2}$ reached up to 38.6 GPa%, which was higher than most of the reported as-cast high-entropy alloys.

Keywords High-entropy alloys · Mechanical properties · Microstructures · Strain hardening

1 Introduction

Other than traditional alloys that use one or two elements as principal elements [1], high-entropy alloys (HEAs) developed in recent years usually contain five or more principal metallic elements, each ranging from 5 to 35 at.% [2]. And different from the traditional metallurgical theory [3, 4], high-entropy alloys tend to form simple solid solutions rather than many complex phases due to their high mixing entropy [4], which results in many promising properties of the alloy, e.g., high strength and hardness, excellent wear, corrosion and oxidation resistance [5–7], high temperature stability [8] and so on.

Different element compositions will have various impacts on the microstructures and properties of the alloys [9]. Many researchers have regulated one or two elements in high-entropy alloys to study the corresponding influence on the alloy systems, so as to obtain the alloy composition with the best overall performance [10, 11]. For example, in the $(\text{FeCoNiCrMn})_{100-x}\text{Al}_x$ system [11], the crystal structures tend to transform from an FCC phase to a mixture of FCC + BCC phases and then to a single BCC phase with the increase in Al content. The same phase transition can also be found in $\text{Al}_x\text{CoCrFeNiTi}$ [12] alloys. In the $\text{AlCoCrFeNb}_x\text{Ni}$ system [13], the microstructures of the alloy series vary from hypoeutectic to hypereutectic; both the compressive yield strength and Vickers hardness are also affected with increasing Nb content. Research on AlCoCrFeNiMo_x [14] shows that σ phase appears when x is more than 0.1. The strength of alloys is increased because of the precipitation strengthening of σ phase. However the plasticity of the alloys is seriously damaged since the precipitation of σ phase. Studies of CoCrFeNiMo_x [15] and AlCrFeNiMo_x [16] show similar results with AlCoCrFeNiMo_x that addition of Mo atoms will have opposite effects on the strength and ductility of alloys.

Generally, Mo element is a σ phase-forming element. Adding a small amount of Mo element will benefit to high-temperature properties and strength of the alloy, but the

Available online at <http://link.springer.com/journal/40195>.

✉ Zhiqiang Cao
caoqz@dlut.edu.cn

¹ Key Laboratory of Solidification Control and Digital Preparation Technology (Liaoning Province), School of Materials Science and Engineering, Dalian University of Technology, Dalian 116024, China

² Ningbo Institute of Dalian University of Technology, Ningbo 315000, China

plasticity will be severely reduced [14–17]. However, Al element can promote the formation of a hard phase BCC; the phase content in the alloy can be tailored through regulating the Al element [10–12]. Therefore, for the alloy system consisting of five elements Al–Cr–Fe–Ni–Mo, their performance can be kept in a relatively good range by adjusting the content of Al or Mo with relatively large atomic radius.

In this study, the molar ratio of molybdenum is fixed and the effect of Al element on microstructures and mechanical properties of $\text{Al}_x\text{CrFe}_2\text{Ni}_2\text{Mo}_{0.2}$ (x value in molar ratio, from 0.6 to 0.9) alloys has been investigated. The resultant microstructures and tensile property of alloys at ambient temperature due to the variation of Al content have been carefully discussed which can provide reference for further research and applications of this high-entropy alloy system.

2 Experimental

The purity of each raw material used in this study is higher than 99.9%. The $\text{Al}_x\text{CrFe}_2\text{Ni}_2\text{Mo}_{0.2}$ (afterward, the alloys are denoted as Al0.6, Al0.7, Al0.8, Al0.9, respectively, as $x=0.6, 0.7, 0.8, 0.9$) alloys were prepared by arc melting in a water-cooled copper hearth under a Ti-gettered high-purity argon atmosphere; each of them was repeatedly melted at least five times for chemical homogeneity. The solidified ingots were about 25 mm in diameter, 10 mm in thickness and weighed 30 g.

For microstructural observation, samples taken from the ingots were mechanically grounded and polished before composition analysis by electron probe microanalysis (EPMA, JXA-8530F) with a wavelength-dispersive spectrometer (WDS). Then, they were etched in aqua regia for microstructure examination through a scanning electron microscope (SEM, ZEISS supra 55) equipped with an energy-dispersive spectrometer (EDS) and an optical microscope (OLYMPUS GX51) which is a suitable choice to observe the solidified structures of the alloys. The crystal structure was characterized by an X-ray diffractometer (XRD, Empyrean) with Cu-K_α radiation target.

For mechanical evaluation, tensile tests were performed at room temperature using UTM4000 series electronic universal testing machine at initial strain rates of $5 \times 10^{-4}/\text{s}$. Dog bone-shaped samples with a size of 30 mm (gauge length) \times 6 mm (width) \times 2 mm (thickness) were cut by wire machining from 120 g cylindrical ingots which were remelted and cast through vacuum intermediate frequency induction furnace. Before the experiment, the wire cutting marks on the surface of the stretch sheet need to be smoothed with sandpaper. Accurate strain was measured with an extensometer (Epsilon, EAG-025M-0200-S). At least three samples were tested for each composition condition to ensure the reliability of results. The tensile fractured

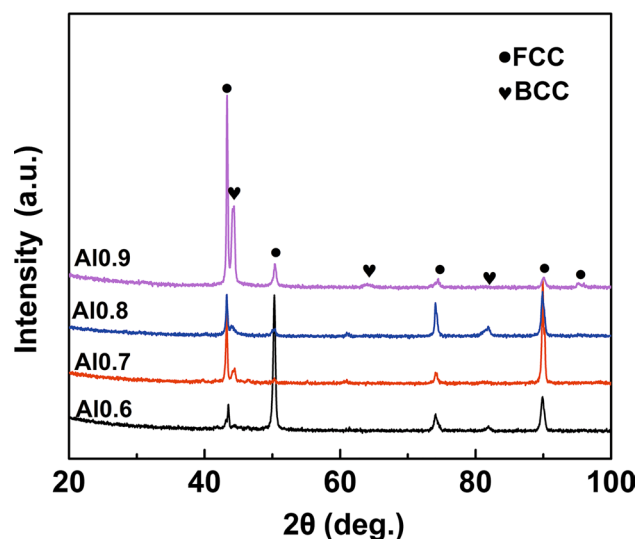


Fig. 1 XRD patterns of the as-cast $\text{Al}_x\text{CrFe}_2\text{Ni}_2\text{Mo}_{0.2}$ high-entropy alloys

Table 1 Parameters of ΔR , ΔH_{mix} , VEC, $\Delta\chi_{\text{Pauling}}$ and $\Delta\chi_{\text{Allen}}$ for $\text{Al}_x\text{CrFe}_2\text{Ni}_2\text{Mo}_{0.2}$ HEAs

Alloys	ΔR (%)	ΔH_{mix} (kJ/mol)	VEC	$\Delta\chi_{\text{Pauling}}$ (%)	$\Delta\chi_{\text{Allen}}$ (%)
Al0.6	4.582	−8.775	7.475	12.56	11.28
Al0.7	4.784	−9.365	7.452	12.74	11.37
Al0.8	4.965	−9.911	7.406	12.90	11.46
Al0.9	5.120	−10.417	7.385	13.04	11.53

samples were isolated from air as much as possible before photographed under SEM. Hardness measurements were taken on a Vickers hardness tester (MH-50) under a load of 1000 g for 15 s. Five measurements were taken with the average value as the result.

3 Results and Discussion

3.1 Microstructural Characteristics

Figure 1 shows the XRD patterns of the as-cast $\text{Al}_x\text{CrFe}_2\text{Ni}_2\text{Mo}_{0.2}$ alloys. It can be found that both FCC and BCC phases exist in all alloys, but the peak strength and position of the BCC phase are different. The two-phase composition of alloys is in line with the expectations of our experimental design. Table 1 shows several common parameters for predicting the phase composition of high-entropy alloys. ΔR is the average atomic radius difference, ΔH_{mix} is the mixing enthalpy, VEC is the valence electron concentration, and $\Delta\chi$ is the electronegativity difference, which are defined by Eqs. (1–4) [18].

$$\Delta R = \sqrt{\sum_{i=1}^n c_i(1 - r_i/\bar{r})^2}, \quad (1)$$

where $\bar{r} = \sum_{i=1}^n c_i r_i$, c_i and r_i are the atomic percentage and atomic radius of the i th element.

$$\Delta H_{\text{mix}} = \sum_{i=1, i \neq j}^n \Omega_{ij} c_i c_j, \quad (2)$$

where $\Omega_{ij} = 4\Delta H_{\text{AB}}^{\text{mix}}$, $\Delta H_{\text{AB}}^{\text{mix}}$ is the mixing enthalpy of binary liquid A–B alloys.

$$\text{VEC} = \sum_{i=1}^n c_i (\text{VEC})_i, \quad (3)$$

where $(\text{VEC})_i$ is the valence electron concentration of the i th element.

$$\Delta\chi = \sqrt{\sum_{i=1}^n c_i(\chi_i - \bar{\chi})^2}, \quad (4)$$

where $\bar{\chi} = \sum_{i=1}^n c_i \chi_i$, χ_i is the Pauling/Allen electronegativity of the i th element.

Dong has summarized the range of parameters predicted to form dual-phase FCC + BCC based on the existing alloy data [19]: $4.7\% \leq \Delta R \leq 6.2\%$, $-13.1 \text{ kJ/mol} \leq \Delta H \leq -2.7 \text{ kJ/mol}$, $7.1 \leq \text{VEC} \leq 8.2$, $\Delta\chi_{\text{Pauling}} \leq 14.6\%$, $\Delta\chi_{\text{Allen}} \leq 16\%$. It is found that the calculated results in Table 1 are very close to the experimental results except that ΔR of Al0.6 differs slightly from the predicted value only by 0.12%. On the other hand, the lattice constants are estimated based on Fig. 1 and listed in Table 2. Obviously, with the addition of Al element, the diffraction peaks of BCC phase gradually become stronger. Namely, the amount of BCC phase in the matrix correspondingly increases. It is also worth noting that the lattice constant of the FCC phase shows a trend of rising primarily and then falling; finally, it remains basically unchanged. This phenomenon is related to the addition of Al with a large atomic radius, which changes the phase distribution and will be discussed in the following text.

To further investigate the phase formation in Al_xCrFe₂Ni₂Mo_{0.2} HEAs, both optical micrographs and SEM images of Al_xCrFe₂Ni₂Mo_{0.2} HEAs are shown in

Table 2 Lattice constant of Al_xCrFe₂Ni₂Mo_{0.2} HEAs

Alloys	FCC (Å)	BCC (Å)
Al0.6	3.5997	2.8886
Al0.7	3.6205	2.8803
Al0.8	3.6182	2.8920
Al0.9	3.6150	2.8862

Figs. 2 and 3, respectively. Figure 2 shows that with the increasing addition of Al element, the solidified structure evolves from dendritic into columnar grains, and finally back to dendritic grains again. Al0.6 and Al0.7 exhibit dendritic structure, as shown in Fig. 2a, b. Figure 3a, b shows the microstructures of Al0.6 and Al0.7. Combined with the XRD result, it can be inferred that the region A corresponds to the FCC phase matrix, and the interdendritic region B is a mixture of FCC phase and BCC phase. According to the enlarged microstructure in the upper right corners, it can be seen that the FCC phase presents a woven network structure with BCC phase, which is also observed in Al0.8 and Al0.9 (see region B in Fig. 3c, d). The chemical composition of region A and B in Al0.6 and Al0.7 probed by WDS is listed in Table 3. It should be noted that region A, which is composed of FCC phase, mainly contains three elements, i.e., Fe, Cr and Ni. According to the XRD diffraction results, the BCC phase is NiAl phase. Correspondingly, the segregation of Al is shown in the WDS results. However, the content of Ni does not change obviously according to WDS results due to the existence of the FCC phase in the region B. Many studies have indicated that Mo was not soluble in NiAl phase [20, 21]; thus, it can be speculated that Mo is likely to be enriched in the FCC phase in the B region.

Figure 2c shows different solidification structures of Al0.8 which are close to columnar grains. As can be further observed by close-up view shown in Fig. 3c, there is a needle-like structure that grows from the grain boundaries in a specific direction into the grains and resembles the Widmanstätten structure (region C). Similar structure has been found in titanium alloys [22] and steel [23].

As the amount of Al content increases to $x=0.9$, the solidification structure presents a typical dendritic morphology again, as shown in Fig. 2d. Notably, little component segregation occurs in Al0.9, which is in accordance with its microstructure in Fig. 3d. There are two different woven mesh structures in Fig. 3d, which is irregular woven mesh structures in region B and the relatively regular one in region D. Such a fine FCC/BCC morphology (~200 nm) has not been reported yet in Al-containing HEAs, which is similar to some BCC/B2 morphology in HEAs with higher Al content [4, 24].

In order to further disclose the distribution of the elements in the two phases, EPMA mapping of Al0.6 was performed as seen in Fig. 4. It is found that the distribution of the elements matches the WDS results very well. Namely, Fe element is mainly enriched in the FCC phase (Fig. 4d), Cr element is mildly segregated in region B (Fig. 4c), and Al and Mo elements are mainly distributed in the interdendritic region (Fig. 4b, f). Figure 4e shows that the Ni element segregates to a certain extent on the edge of the dendrite consisting of black-stripe BCC phases. According to Table 4, the lower mixing enthalpy of Al atom and

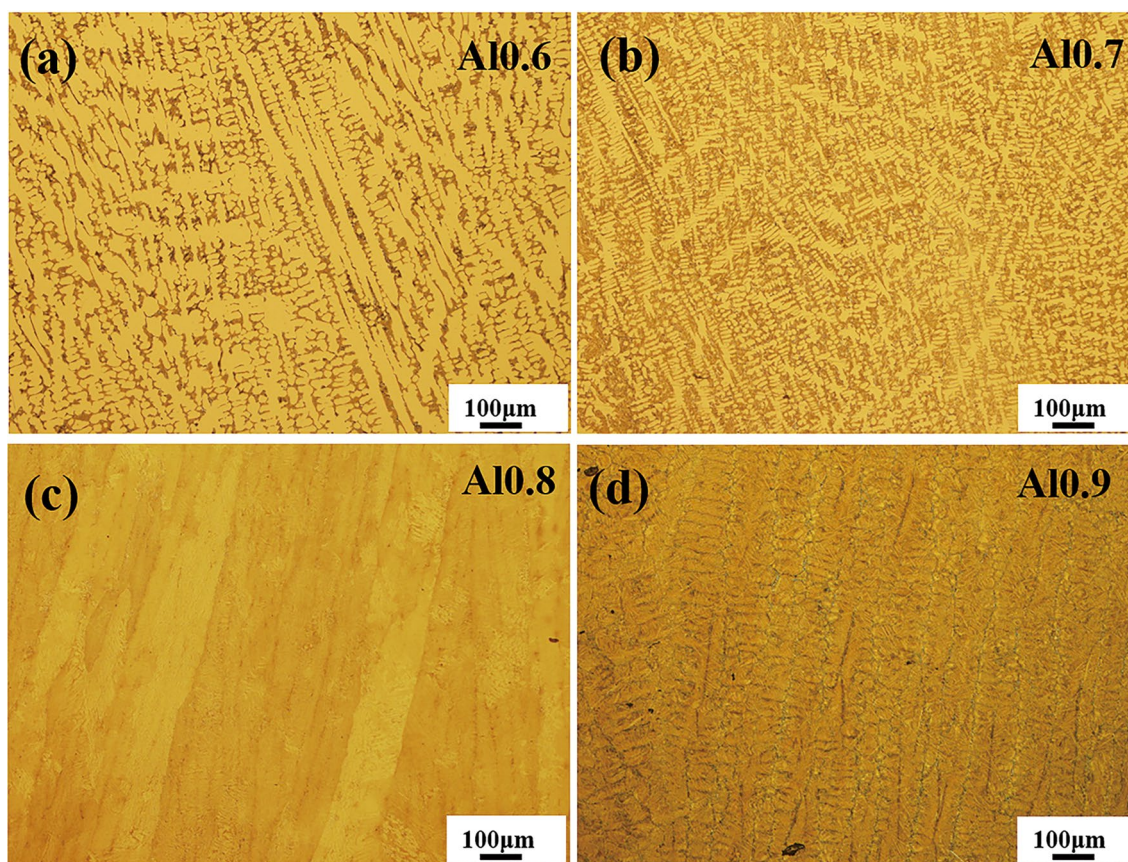


Fig. 2 Optical micrographs of as-cast $\text{Al}_x\text{CrFe}_2\text{Ni}_2\text{Mo}_{0.2}$ alloys showing microstructural evolution from dendrite **a**, **b** to columnar grains **c**, then to dendrite with little component segregation **d**

Ni atom indicates that the strongest attractive force exists between these two atoms. During the solidification of the FCC matrix, Al and Ni atoms with lower melting point will be repelled to the front of the solidification interface, which makes it more convenient for the formation of the AlNi phase [4]. It is worth noting that the Mo-enriched region (Fig. 4f) coincides with the white-color parts in the interdendritic region (Fig. 4a), indicating that Mo atoms tend to dissolve into the FCC phase, which confirms the conjecture above. Since Mo atom is not soluble in AlNi phase, during solidification, more Mo atoms tend to be dissolved into the FCC phase for a high percentage of BCC specimens, and vice versa. With the addition of Al element ($x=0.8$, $x=0.9$), the fraction of BCC phase increases, and less FCC phase forms. At last, the Mo content of the FCC phase in the alloy tends to be rich for a high percentage of BCC organizations. Caused by the formation of BCC phase, it is difficult to judge the solid solubility of Al atoms in FCC phase. Therefore, in the high-entropy alloy with variable Al content, the FCC lattice constant usually appears irregular fluctuations [4, 11]. The existence of Mo atom will make the lattice constant increase, but

the formation of BCC phase will make the FCC lattice constant uncertain.

Generally, the solidification morphology of an alloy is affected by many factors, such as the cooling rate of the alloy, the temperature gradient at the front of the solid–liquid interface, the degree of undercooling, the solute concentration and so on. For alloys with similar cooling conditions, the alloy compositions will have a certain effect on the resultant solidified structure. For example, in this alloy system, Al0.8 shows a different solidification morphology from other alloys, which mainly caused by the small constituent supercooling during the solidification process. Consequently, Al0.8 will exhibit cellular growth rather than dendritic growth. Therefore, we can infer that Al0.8 has the smallest solidification temperature range in the alloy system.

3.2 Mechanical Properties

Up to now, tensile properties at room temperature are less reported than the compressive properties of as-cast HEAs [25], and the tensile properties of molybdenum-containing alloys are even less reported [26, 27]. In order to study the

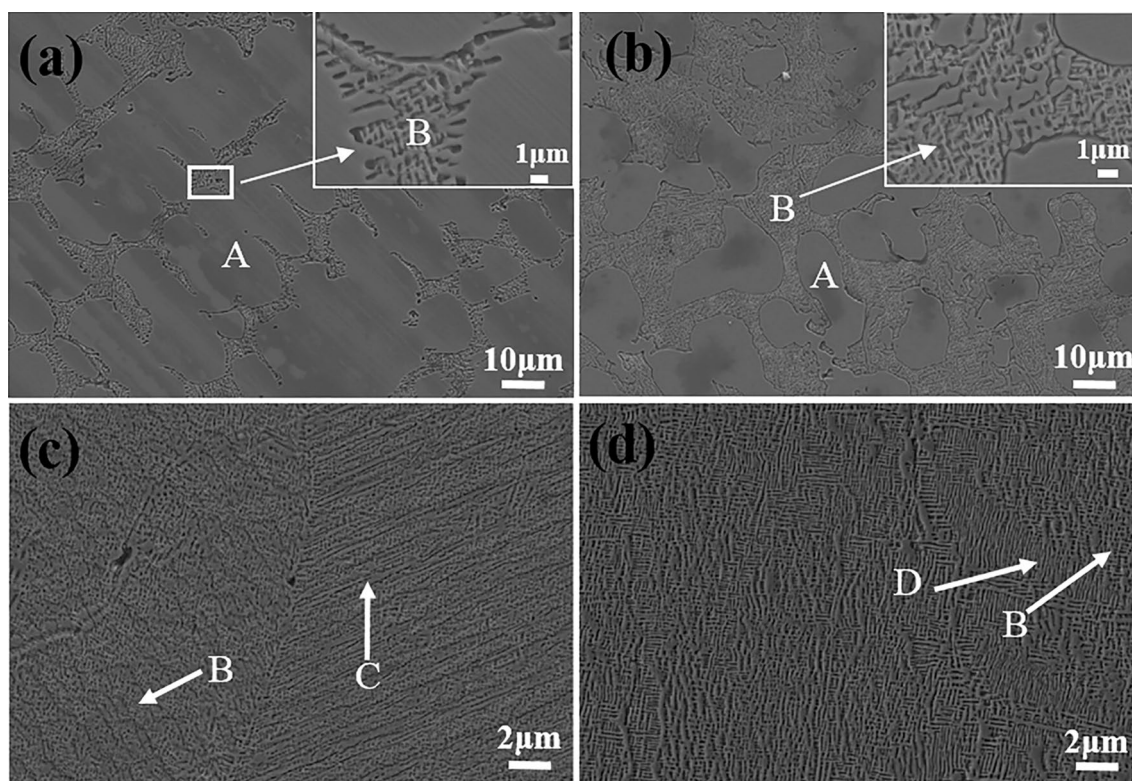


Fig. 3 SEM images of as-cast $\text{Al}_x\text{CrFe}_2\text{Ni}_2\text{Mo}_{0.2}$ alloys: **a** $x=0.6$, **b** $x=0.7$, **c** $x=0.8$, **d** $x=0.9$

Table 3 WDS results of Al0.6 and Al0.7 in different regions

Alloy	Spectrum point	Al	Cr	Fe	Ni	Mo
Al0.6	A	8.36	17.90	39.18	31.97	2.58
	B	14.03	18.10	29.51	33.78	4.57
Al0.7	A	8.98	17.96	38.57	31.91	2.58
	B	14.09	19.13	31.84	30.86	4.09

influence of microstructures on mechanical properties, uniaxial tensile tests are conducted. Figure 5a shows the tensile engineering stress–strain curves of $\text{Al}_x\text{CrFe}_2\text{Ni}_2\text{Mo}_{0.2}$ alloys. The extracted tensile yield strength (σ_{yt}), fracture strength (σ_{bt}) and elongation (ϵ_t) are listed in Table 5. With the increase in Al content, the growth of σ_{yt} and σ_{bt} is divided into three stages: slight increase from Al0.6 to Al0.7; significant improvement from Al0.7 to Al0.8 and almost unchanged from Al0.8 to Al0.9. However, the ductility of alloys suffers severe damage with increasing Al content. The ϵ_t of Al0.7 was only half that of Al0.6, and the ϵ_t of Al0.8 and Al0.9 dropped only to 9%.

$\text{Al}_x\text{CrFe}_2\text{Ni}_2\text{Mo}_{0.2}$ alloys have FCC + BCC dual-phase structure, and the BCC phase exhibits the characteristics of “brittle and hard” mechanical property, while the FCC phase is more “soft and tough.” The previous study on the deformation mechanisms of $\text{AlCoCrFeNi}_{2.1}$ with FCC + BCC dual-phase structure indicated that solid

solution hardening and semi-coherent phase boundaries contributed to the high strength of the alloys by pinning massive dislocations [28]. For $\text{Al}_x\text{CrFe}_2\text{Ni}_2\text{Mo}_{0.2}$ alloys, the two-phase interface increases with the increasing BCC phase. The phase interface will impede the motion of dislocation during deformation, which improves the strength of the alloys. It can be seen from Figs. 3 and 5 that when $x=0.8$ and 0.9, due to the close combination of the two phases, the strength of the alloys shows a sudden change as compared to when $x=0.7$.

The tensile yield strength, hardness HV and the volume fraction of BCC phase estimated by Image Pro Plus are plotted in Fig. 6 as a function of x in $\text{Al}_x\text{CrFe}_2\text{Ni}_2\text{Mo}_{0.2}$. It can be found that all three variables show similar trend with the increase in x . Consequently, the volume fraction of BCC phase plays a major role in improving the yield strength and hardness of the alloys which is consistent with the above discussion.

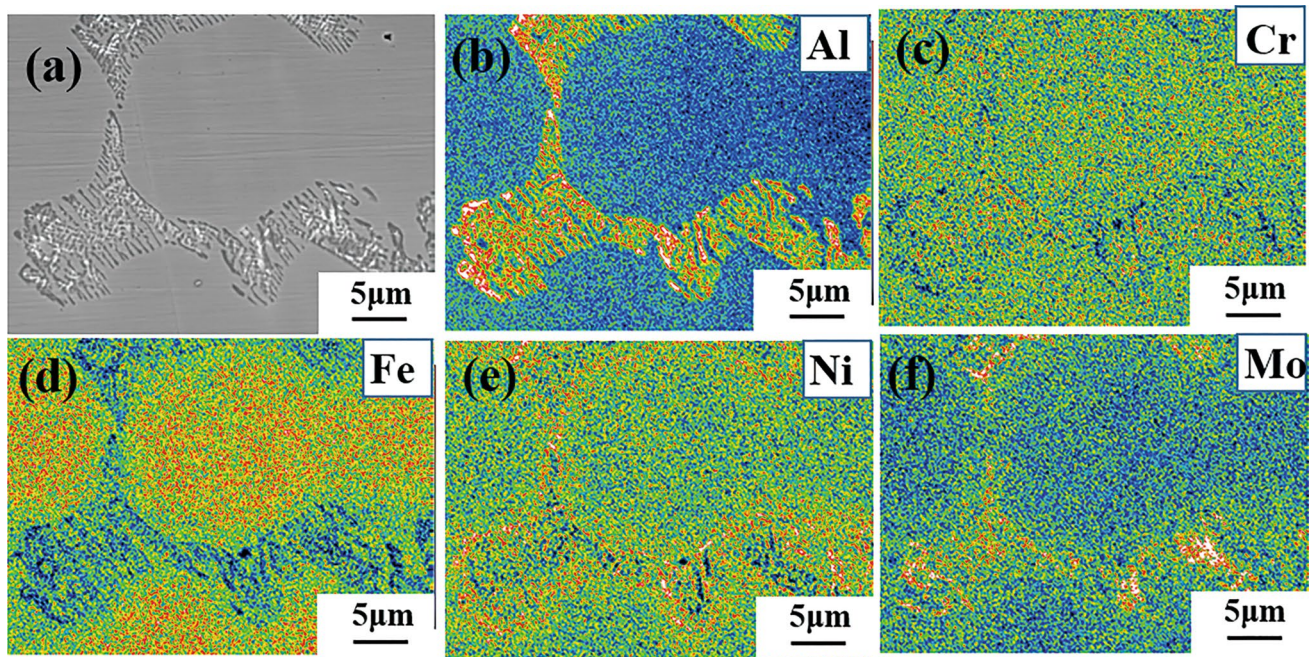


Fig. 4 EPMA mapping of Al_{0.6}: **a** backscattered electron image, **b** Al, **c** Cr, **d** Fe, **e** Ni, **f** Mo

Table 4 Chemical mixing enthalpy of the atomic pairs

	Al	Cr	Fe	Ni	Mo
Al	-	-	-	-	-
Cr	-10	-	-	-	-
Fe	-11	-1	-	-	-
Ni	-22	-7	-2	-	-
Mo	-5	0	-2	-7	-

Figure 7 shows the fracture morphology of Al_xCrFe₂Ni₂Mo_{0.2}. Apparently, Al_{0.6} and Al_{0.7} show ductile fracture characteristics. Compared with Al_{0.7}, the dimple distribution of Al_{0.6} is more uniform, and the Al_{0.6} shows the typical dendritic fracture morphology with the trace of the softer phase being torn. For Al_{0.8} and Al_{0.9} in Fig. 7c, d, the dimples are very shallow, and the fracture surface is bright and stepped, indicating a more brittle fracture mode.

After comparative analysis of the comprehensive properties of the alloys, it is seen that Al_{0.6} exhibits excellent comprehensive mechanical properties. In order to understand the ductile effect of the alloys, we have carefully assessed the work hardening rate (dS/de), and the strain hardening exponent (n) of the alloys is calculated from the true stress–strain curve obtained at room temperature. It is known that the true stress–strain curve (Fig. 5b) is assumed to be expressed by the Hollomon equation:

$$S = Ke^n, \quad (5)$$

where K is coefficient of hardening, and n is referred to the work hardening exponent. The formula can be converted to a logarithmic form:

$$\ln S = \ln K + n \ln e. \quad (6)$$

The higher n value is usually associated with the higher level of strengthening and toughness which effectively alleviates the localized deformation (inhibit crack formation and propagation) and enhances the uniform elongation under complex stress conditions. The work hardening exponent n is theoretically a constant; however, it varies with the plastic deformation in certain materials [27, 29].

The strain hardening rates (dS/de) and n values were calculated from the yield to the ultimate tensile strength, and the results are illustrated in Fig. 5c, d. In our research, the ultimate tensile strength of the alloy is equal to the breaking strength caused by non-necking of the alloy, which will be demonstrated below.

Figure 5c shows that the strain hardening rate of the alloys increases with the increasing addition of aluminum. Except for Al_{0.6} which maintains almost constant strain hardening rate of 1.7–1.8 GPa during the uniform plastic deformation stage, the strain hardening rate of other alloys always decreases with increasing strain. Based on the necking criterion, necking occurs when the slope on the true stress–strain is equal to the true stress at that point, i.e., $dS/de = S$ [30]. Obviously, no necking takes place in all alloys,

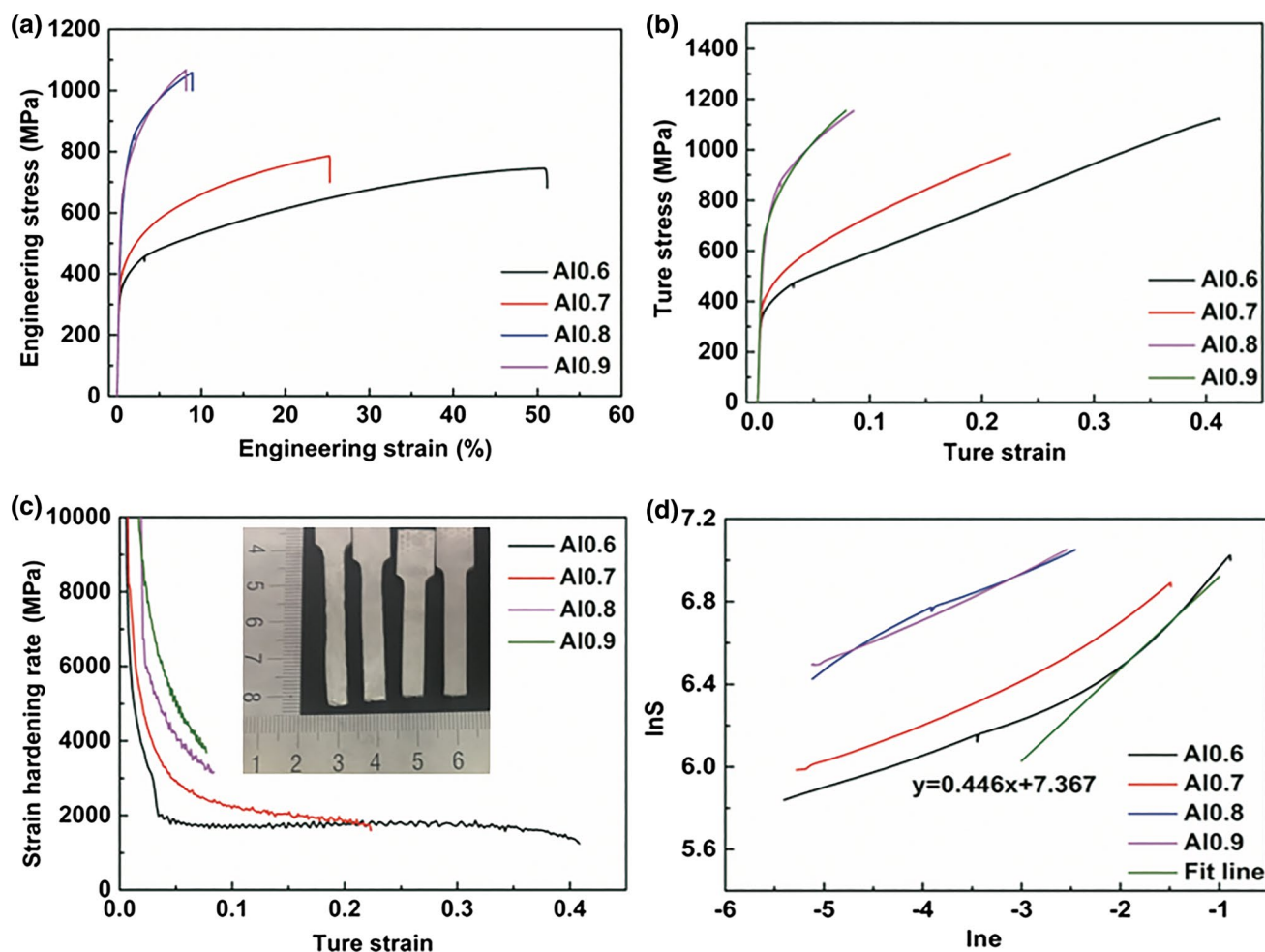


Fig. 5 Engineering **a** and true **b** stress–strain curves, as well as strain hardening rate **c** and $\ln S$ – $\ln \epsilon$ curves **d** of Al_xCrFe₂Ni₂Mo_{0.2} alloys

Table 5 Data summary for Al_xCrFe₂Ni₂Mo_{0.2} alloys, including tensile yield strength σ_{yt} , tensile fracture strength σ_{bt} , tensile elongation ϵ_t , Vickers hardness HV, the volume fraction of BCC phase [BCC (%)] and the product of strength and elongation (GPa%)

Alloy	σ_{yt} (MPa)	σ_{bt} (MPa)	ϵ_t (%)	HV	BCC (%)	Product of strength and elongation (GPa%)
Al0.6	341	744	52	241.52	6.74	38.6
Al0.7	398	785	25	298.17	17.01	19.6
Al0.8	622	1059	9	388.56	38.76	9.5
Al0.9	657	1067	8	397.10	42.43	8.5

that is, the alloy will fracture during the uniform plastic deformation stage. Therefore, their minimum strain hardening rates are still greater than their true tensile strengths. This view is also supported by the tensile fracture shown in Fig. 5c (from left to right: Al0.6, Al0.7, Al0.8 and Al0.9).

From Fig. 5d, we can find that Al0.8 and Al0.9 have equivalent n value of 2.2 ± 0.1 . However, the equations of Al0.6 and Al0.7 do not fit straight lines, indicating that in these two alloys, the work hardening exponent changes with

the increase in deformation. Especially, the n value of Al0.6 varies wildly from the early to the late stage of the deformation which reflects huge transformation of the deformation mechanism in Al0.6 during deformation.

As is well-known, the strain hardening ability is usually related to the alloy's stacking fault energy [31]. FCC metals generally have lower stacking fault energy and a higher work hardening exponent. In Al0.6, the alloy shows a lower work hardening ability in the early stage because

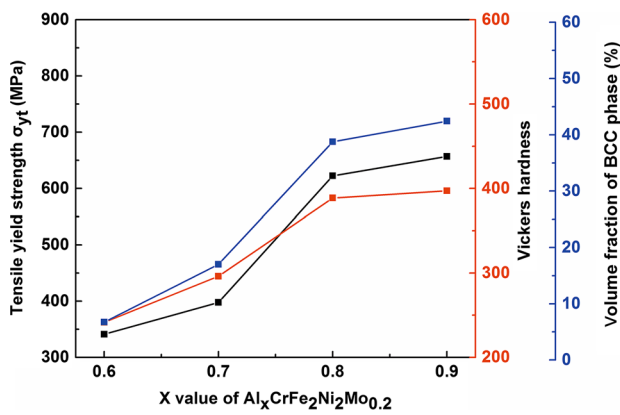


Fig. 6 Tensile yield strength, hardness and the volume fraction of BCC phase with x value of $Al_xCrFe_2Ni_2Mo_{0.2}$

of the dislocation slip deformation. With deformation progresses, deformation-induced stacking faults may occur in the alloy, resulting in a significant improvement in its work hardening ability. Stacking faults are considered to be important crystal defects that affect mechanical properties at room temperature [32]. The intersecting stacking

fault bands have similar effect with grain size refinement, which could be a reason for excellent tensile stress and ductility of Al0.6 [33–35]. Moreover, necking is associated with the work hardening ability of alloys. The necking is caused by the uneven deformation of the material. When the work hardening is slower than the change of external stress, the local deformation of the material will be activated and lead to necking. It is the improvement of work hardening ability during the deformation process that makes Al0.6 and Al0.7 show great toughness without necking.

As for Al0.8 and Al0.9, numerous BCC phase would inevitably cause embrittlement of the alloys. Especially in Al0.8, the existence of tissues similar to Widmanstätten structure causes the matrix to split, which may lead to great loss of plasticity. High hardening rate and low hardening capacity can also bring about the reduction of plasticity for both alloys. In addition, the decreasing work hardening rate throughout the plastic deformation process and the constant hardening exponent of both alloys indicate that the deformation of these two alloys takes place mainly via dislocation slip [27]. Dislocations encountered a large number of grain boundaries and solid

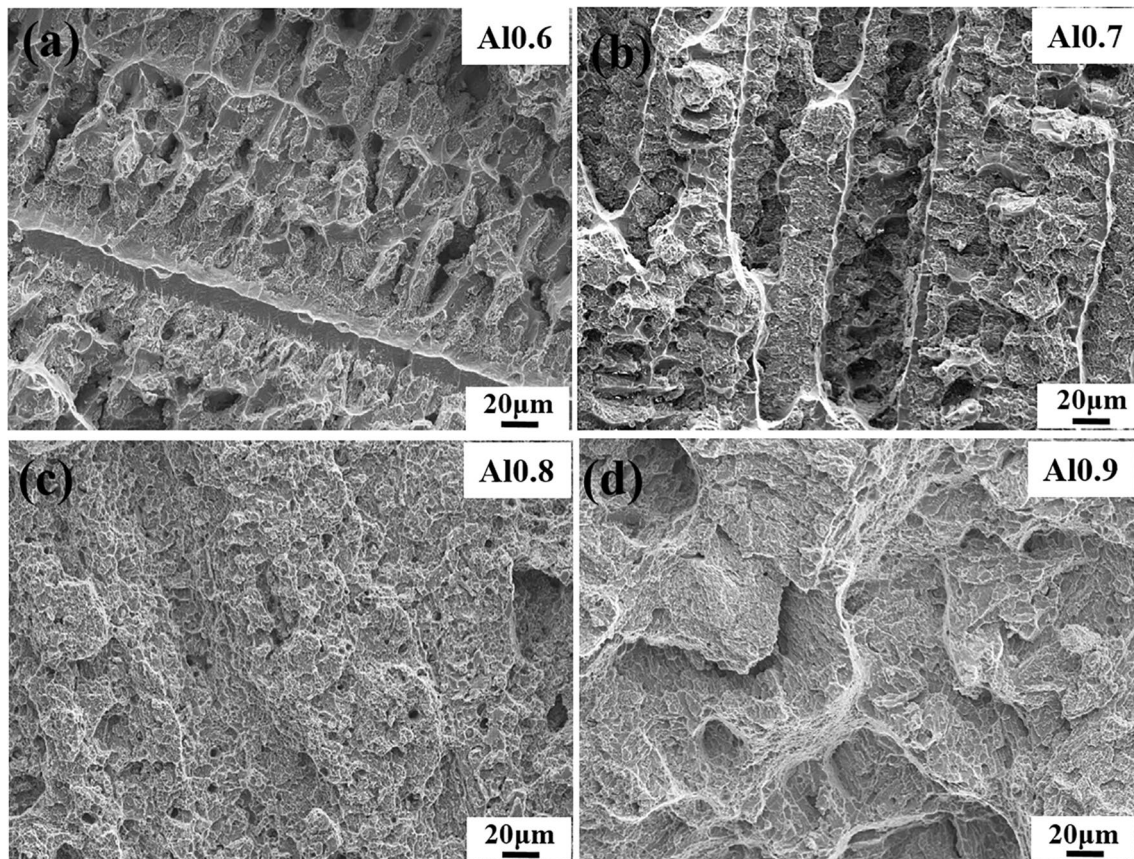


Fig. 7 Fracture morphologies of $Al_xCrFe_2Ni_2Mo_{0.2}$: **a** Al0.6, **b** Al0.7, **c** Al0.8, **d** Al0.9

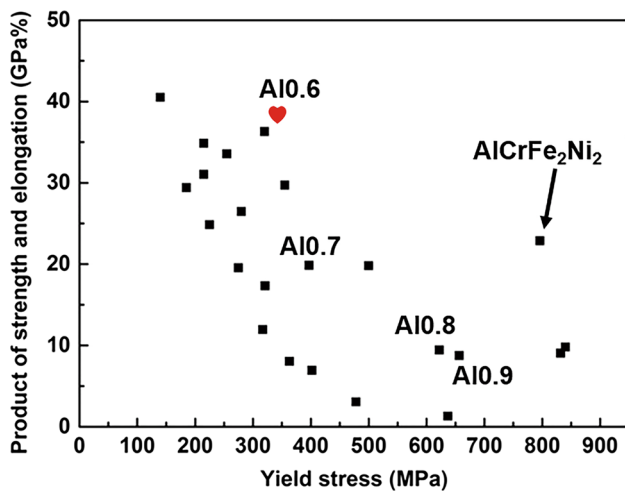


Fig. 8 Yield stress versus product of strength and elongation for the reported as-cast high-entropy alloys in the engineering stress–strain condition

solution atoms during the slip process, forming dislocation entanglements, which results in a higher strength and meanwhile great loss of plasticity in the alloy.

Furthermore, the product of strength and elongation of $\text{Al}_x\text{CrFe}_2\text{Ni}_2\text{Mo}_{0.2}$ is listed in Table 5. The comparison of yield strength and the product of strength and elongation with some other as-cast high-entropy alloys [11, 28, 31, 36–44] is summarized in Fig. 8. It is clear that Al0.6 has excellent comprehensive mechanical properties due to the above-mentioned special deformation mechanism. And its product of strength and elongation reaches up to 39 GPa%, which is higher than most of the reported as-cast high-entropy alloys.

4 Conclusions

1. The microstructures with dual phases of FCC + BCC are formed in $\text{Al}_x\text{CrFe}_2\text{Ni}_2\text{Mo}_{0.2}$ with the x value from 0.6 to 0.9. And solidified structures change from dendrite (Al0.6, Al0.7) to columnar grain (Al0.8) then back to dendrite (Al0.9) again. With the increase in the Al content, the volume fraction of the BCC phase increases, and the distribution of two-phase microstructure becomes more uniform. The woven mesh structure can be observed in the entire Al0.9, and the width of the two phases is only about 200 nm.
2. Results of tensile experiments show that the yield strength increases from 341 to 657 MPa, but the plasticity is severely reduced from 52% at Al0.6 to 8% at Al0.9. The increasing BCC phase and its nearly uniform distribution in Al0.8 and Al0.9 generate more two-phase

interfaces, which increases the resistance of deformation and thus improves the strength of both alloys.

3. Strain hardening rates increase from Al0.6 to Al0.9; among them, Al0.6 has a most stable strain hardening rate of 1.7–1.8 GPa during the whole stage of uniform plastic deformation. Higher hardening capacity and stable strain hardening rate make Al0.6 excellent plasticity without necking.
4. The product of strength and elongation of Al0.6 reaches up to 38.6 GPa% which is higher than most of reported as-cast high-entropy alloys.

Acknowledgements This work was financially supported by the National Key Research and Development Program of China (No. 2017YFA0403803) and the National Natural Science Foundation of China (Nos. 51771041 and 51901116).

References

- [1] ASM, *ASM Handbook, Vol. 1: Alloy Phase Diagrams*, 10th edn. (ASM International, Materials Park, 1992), p. 949
- [2] D.B. Miracle, O.N. Senkov, *Acta Mater.* **122**, 448 (2017)
- [3] A.L. Greer, *Nature* **366**, 303 (1993)
- [4] W.R. Wang, W.L. Wang, S.C. Wang, Y.C. Tsai, C.H. Lai, J.W. Yeh, *Intermetallics* **26**, 44 (2012)
- [5] Y.P. Cai, G.J. Wang, Y.J. Ma, Z.H. Cao, X.K. Meng, *Scr. Mater.* **162**, 281 (2019)
- [6] A. Verma, P. Tarate, A.C. Abhyankar, M.R. Mohape, D.S. Gowtam, V.P. Deshmukh, T. Shanmugasundaram, *Scr. Mater.* **161**, 21 (2019)
- [7] S.J. Zheng, Z.B. Cai, J.B. Pu, C. Zeng, S.Y. Chen, R. Chen, L.P. Wang, *Appl. Surf. Sci.* **483**, 870 (2019)
- [8] H.M. Daoud, A.M. Manzoni, N. Wanderka, U. Glatzel, *JOM* **67**, 2271 (2015)
- [9] C. Xiang, Z.M. Zhang, H.M. Fu, E.H. Han, J.Q. Wang, H.F. Zhang, G.D. Hu, *Acta Metall. Sin. (Engl. Lett.)* **32**, 1053 (2019)
- [10] Y.X. Zhuang, X.L. Zhang, X.Y. Gu, *J. Alloys Compd.* **743**, 514 (2018)
- [11] J.Y. He, W.H. Liu, H. Wang, Y. Wu, X.J. Liu, T.G. Nieh, Z.P. Lu, *Acta Mater.* **62**, 105 (2014)
- [12] K.B. Zhang, Z.Y. Fu, *Intermetallics* **22**, 24 (2012)
- [13] S.G. Ma, Y. Zhang, *Mater. Sci. Eng. A* **532**, 480 (2012)
- [14] Y. Dong, Y.P. Lu, J.R. Kong, J.J. Zhang, T.J. Li, *J. Alloys Compd.* **573**, 96 (2013)
- [15] J.M. Zhu, H.M. Fu, H.F. Zhang, A.M. Wang, H. Li, Z.Q. Hua, *Mater. Sci. Eng. A* **527**, 6975 (2010)
- [16] T.T. Shun, L.Y. Chang, M.H. Shiu, *Mater. Charact.* **70**, 63 (2012)
- [17] J.M. Zhu, H.F. Zhang, H.M. Fu, A.M. Wang, H. Li, Z.Q. Hu, *J. Alloys Compd.* **497**, 52 (2010)
- [18] S. Guo, C.T. Liu, *Prog. Nat. Sci. Mater. Int.* **21**, 434 (2011)
- [19] Y. Dong, Dissertation, Dalian University of Technology, 2016 (**in Chinese**)
- [20] L. Wang, J. Shen, Z. Shang, H.Z. Fu, *Scr. Mater.* **89**, 2 (2014)
- [21] L. Wang, C.L. Yao, J. Shen, Y.P. Zhang, T. Wang, H.X. Xu, L.H. Gao, G.J. Zhang, *Mater. Sci. Eng. A* **744**, 596 (2019)
- [22] D.G. Lee, S. Lee, Y.T. Lee, *Mater. Sci. Eng. A* **486**, 21 (2008)
- [23] J.R. Yang, L.C. Chang, *Mater. Sci. Eng. A* **223**, 158 (1997)
- [24] Y. Ma, Q. Wang, B.B. Jiang, C.L. Li, J.M. Hao, X.N. Li, C. Dong, T.G. Nieh, *Acta Mater.* **147**, 217 (2018)

- [25] Z.Y. Rao, X. Wang, J. Zhu, X.H. Chen, L. Wang, J.J. Si, Y.D. Wu, X.D. Hui, *Intermetallics* **77**, 23 (2016)
- [26] B. Cai, B. Liu, S. Kabra, Y.Q. Wang, K. Yan, P.D. Lee, Y. Liu, *Acta Mater.* **127**, 471 (2017)
- [27] W.H. Liu, Z.P. Lu, J.Y. He, J.H. Luan, Z.J. Wang, B. Liu, Y. Liu, M.W. Chen, C.T. Liu, *Acta Mater.* **116**, 332 (2016)
- [28] X.Z. Gao, Y.P. Lu, B. Zhang, N.N. Liang, G.Z. Wu, G. Sha, J.Z. Liu, Y.H. Zhao, *Acta Mater.* **141**, 59 (2017)
- [29] T. Xu, Y. Feng, Z. Jin, S. Song, D. Wang, *Mater. Sci. Eng. A* **550**, 80 (2012)
- [30] Q. Li, T.W. Zhang, J.W. Qiao, S.G. Ma, D. Zhao, P. Lu, B. Xu, Z.H. Wang, *Mater. Sci. Eng. A* **767**, 138424–138426 (2019)
- [31] M.V. Klimova, A.O. Semenyuk, D.G. Shaysultanov, G.A. Salishchev, S.V. Zherebtsov, N.D. Stepanov, *J. Alloys Compd.* **811**, 15200–15206 (2019)
- [32] Z.R. Pei, *Mater. Sci. Eng. A* **737**, 132 (2018)
- [33] W.Y. Huo, H. Zhou, F. Fang, X.J. Hu, Z.H. Xie, J.Q. Jiang, *Mater. Sci. Eng. A* **689**, 368 (2017)
- [34] K. Rajan, J.B. Sande, *J. Mater. Sci.* **17**, 769 (1982)
- [35] K. Rajan, *Metall. Trans. A* **13**, 1161 (1982)
- [36] Y. Dong, X.X. Gao, Y.P. Lu, T.M. Wang, T.J. Li, *Mater. Lett.* **169**, 62 (2016)
- [37] W.H. Liu, J.Y. He, H.L. Huang, H. Wang, Z.P. Lu, C.T. Liu, *Intermetallics* **60**, 1 (2015)
- [38] S.G. Ma, S.F. Zhang, J.W. Qiao, Z.H. Wang, M.C. Gao, Z.M. Jiao, H.J. Yang, Y. Zhang, *Intermetallics* **54**, 104 (2014)
- [39] G.A. Salishchev, M.A. Tikhonovsky, D.G. Shaysultanov, N.D. Stepanov, A.V. Kuznetsov, I.V. Kolodiy, A.S. Tortika, O.N. Senkov, *J. Alloys Compd.* **591**, 11 (2014)
- [40] C. Ng, S. Guo, J.H. Luan, Q. Wang, J. Lu, S.Q. Shi, C.T. Liu, *J. Alloys Compd.* **584**, 530 (2014)
- [41] S.Z. Niu, H.C. Kou, T. Guo, Y. Zhang, J. Wang, J.S. Li, *Mater. Sci. Eng. A* **671**, 82 (2016)
- [42] T.T. Zou, S.B. Ren, P.K. Liaw, Y. Zhang, *Int. J. Miner. Metall. Mater.* **20**, 549 (2013)
- [43] X. Jin, Y.X. Liang, L. Zhang, J. Bi, Y. Zhou, B.S. Li, *Mater. Sci. Eng. A* **745**, 137 (2019)
- [44] N.D. Stepanov, N.Y. Yurchenko, M.A. Tikhonovsky, G.A. Salishchev, *J. Alloys Compd.* **687**, 59 (2016)